Fabrication of Brushite Coating on AZ91D and AZ31 Alloys by Two-Step Chemical Treatment and Its Surface Protection in Simulated Body Fluid

Y. Sasikumar, A. Madhan Kumar, R. Suresh Babu, P. Dhaiveegan, N. Al-Aqeeli, and Ana L.F. de Barros

A biocompatible dicalcium phosphate dihydrate (DCPD) brushite coating of flake-like crystals was developed on AZ91D and AZ31 magnesium (Mg) surfaces to control and slow down the rapid degradation rate of the substrates. The electrochemical behavior of the DCPD-coated substrates was examined in a simulated body fluid (SBF) with uncoated substrates as the control. Fabrication of the coating was achieved via chemical immersion technique by modifying the surfaces with $Ca(NO_3)_2 \cdot 4H_2O$ and KH_2PO_4 in addition to heat treatment. The morphology of the DCPD coating is uniform and dense with a flake-like crystal structure. After in vitro tests, the DCPD coating would have exhibited excellent corrosion resistance with more biomineralization of the active calcium phosphate (CaP). Moreover, the DCPD coating induced CaP formation after immersion in the SBF, indicating excellent bioactivity upon increasing the coating. Hence, the two-step chemical treatment enhances the bioactivity of DCPD coatings on Mg alloys, making them better implant materials.

Keywords	biocompatibility, coating, DCPD, Mg alloys, SBF

1. Introduction

Magnesium (Mg) and its alloys are considered as a promising material for the next-generation degradable orthopedic implant and received more attention in recent years due to their excellent biocompatibility and corrosion resistance with suitable mechanical properties. However, the poor biological activity and fast degradation rate in the human body environment have limited their applications to artificial bioimplant materials for the treatment of heart and other bone diseases. No infections were observed, when these biomedical implant materials have been operated in the human body. However, the major drawback is the fast degradation rate observed in the pH range (7.4-7.6) with high chloride content (of approximately 150 mmol^{-1}) in a living human body. An occurrence of rapid hydrogen gas evolution during the corrosion process leads to a mechanical integrity loss before the completion of healing tissues (Ref 1-3). Mg alloys can be used worldwide, if their corrosion resistance is increased.

Suitable nontoxic elements such as Ca, Zn, Mn, Zr and Al were added to reduce the fast degradation rate of the Mg alloys. Generally, aluminum and zirconium have been used as the main alloying elements (Ref 4). Alloying elements play a major role in improving and influencing the physical, chemical and mechanical properties of Mg alloys. Aluminum has significantly improved the mechanical properties of Mg alloys with the formation of the $Mg_{17}Al_{12}$ phase. The Mn and Zn elements also play a similar role as Al in Mg alloys. The solubility of Zr in magnesium is lower, and Zr has a strong affinity with oxygen; thus, it can form zirconia to refine the grain size of magnesium alloys.

Surface modification methods are one of the most widely used techniques as an effective way to decrease the initial degradation rates in vivo and to maintain the mechanical properties of Mg and its alloys (Ref 5, 6). Among the various coating methods available, the sol–gel coating method has been found to be appropriate for coating Mg alloys to reduce their degradation rate. However, the major drawback of sol–gel coating is the dissolution rate, which is very high; this increases the potential of biomedical implants, which leads to the loosening of the implant from the bone attachment and compromises the in vivo stability (Ref 7-11). Hence, it is the simplest, most cost-effective method with a good bone bonding ability. The surface modification method through the chemical route has found to be a promising method and has received attention because of its application for implants with complicated shapes (Ref 12). Thus, a simple, cost-effective chemical treatment was performed to produce a uniform porous network structure over Mg surfaces to enhance the osseointegration suitable for the orthopedic implants. Surface modification by chemical treatments, such as NaOH (Ref 13) and H_2O_2 (Ref 14), is common for modifying surfaces to improve their corrosion resistance and mechanical stability. Deposition techniques, like CaP treatment, HA coatings, biomimetic techniques (Ref 15), chemical deposition (Ref 15, 16) and electrodeposition (Ref 17-22), are employed. CaP coatings,

Y. Sasikumar, R. Suresh Babu, and Ana L.F. de Barros, Laboratory of Experimental and Applied Physics, Centro Federal de Educação Tecnológica Celso Suckow da Fonseca, Av. Maracanã Campus 229, Rio de Janeiro 20271-110, Brazil; A. Madhan Kumar, Center of Research Excellence in Corrosion, Research Institute, King Fahd University of Petroleum and Minerals, Dhahran 31261, Kingdom of Saudi Arabia; P. Dhaiveegan, Department of Chemical Engineering, Tatung University, No. 40, Sec. 3, Zhongshan, North Rd., Taipei City 104, Taiwan; and N. Al-Aqeeli, Department of Mechanical Engineering, King Fahd University of Petroleum and Minerals, Dhahran 31261, Kingdom of Saudi Arabia. Contact e-mail: madhankumar@kfupm.edu.sa.

including HA, DCPD and TCP, offer good biocompatibility and bioactivity due to the main elements such as Ca and P, which have been present in natural bone. Hence, DCPD and HA are the most preferred materials used for coatings because of their chemical and structural resemblance similar to human natural bone, which can accelerate bone concrescence (Ref 22).

Bioactive surface modification of carbon/carbon composites with multilayer SiC nanowire-Si-doped hydroxyapatite coating with a controllable preparation and its oxidation damage of SiC-coated carbon fiber-reinforced hydroxyapatite composites have been studied by various researchers (Ref 23-25).

Preparation and characterization of carbon/SiC, nanowire/Na-doped carbonated hydroxyapatite multilayer coating for C–C composites (Ref 26), Sr and Na co-substituted hydroxyapatite coatings for carbon/carbon composites (Ref 27), Sr and Mg co-substituted dicalcium phosphate dehydrate coating for carbon/carbon composites by pulsed electrodeposition (Ref 28), pyrolytic carbon-SiC-fluoridated hydroxyapatite multilayered coating on carbon fibers (Ref 29) have been reported by various researchers.

The coating employed on magnesium and its alloys should be bioactive with good biocompatibility of the osteoconductive CaP coating. The main objective of this investigation was to fabricate DCPD coating via chemical immersion technique on the surface of AZ91D and AZ31 alloys and its electrochemical corrosion behavior in an SBF solution. Furthermore, in vitro studies were carried out for the AZ91D and AZ31 alloys in SBF for long-term implant applications.

2. Materials and Methods

2.1 Substrate Preparation and Cleaning

AZ91D and AZ31Mg alloys with dimensions of 1×1 cm^2 were used as the substrates, and their chemical compositions are given in Table 1. All the substrates were mechanically polished using SiC-coated abrasive emery papers with a 2500 grit to obtain a homogeneous roughness. After grinding, the substrates were ultrasonically cleaned with acetone to remove the residue materials present on the substrates. Furthermore, the substrates were thoroughly rinsed and gently washed with distilled water and then dried at room temperature. The residue-free cleaned substrates were chemically etched with HCl:H$_2$O mixture in the ratio of 1:4 (in volume) at 60 °C for 2 min to remove the oxide layer formed on the substrates. Additionally, ultrasonic cleaning was performed in distilled water for approximately 15 min; further, they were dried.

2.2 Surface Treatment via Chemical Deposition

The chemical conversion coatings were fabricated by two-step process. Step 1: All rinsed and cleaned substrates were pretreated with NaOH by immersing the substrates with 40 mL aqueous solution of 1 M NaOH at 60 °C for 24 h in an oven and gently washed with distilled water. Step 2: After the pretreatment process, the substrates were removed from the NaOH solution and thoroughly washed with distilled water and dried. The dried substrates were immersed in 40 mL of an aqueous solution containing 0.1 M Ca(NO$_3$)$_2$·4H$_2$O and 0.05 M KH$_2$PO$_4$ in 500 mL of deionized water at 80 °C for 2 h. Hence, the two-step chemical treatment was performed. DCPD coatings were fabricated on the substrates. Further, the substrates were thoroughly rinsed and washed with distilled water and dried. The dried substrates were further subjected to heat treatment using an airtight electric furnace kept at 400 °C for 1 h. Finally, the substrates were allowed to cool until reaching room temperature inside the furnace. The thickness of the DCPD or brushite coatings was measured by a coating thickness gauge (Elcometer Instruments, Germany), and the error in the thickness measurements was less than 5%. The average thickness of DCPD coatings was found to be about 14-15 μm, respectively.

2.3 In Vitro Corrosion Studies

In vitro corrosion experiments for the surface-treated AZ91D and AZ31 alloys were performed to assess the bioactivity of the DCPD coating and CaP growth formation (through immersion tests) by immersing the substrates in SBF solution for a period of approximately 168 h. The electrolyte medium used was the SBF solution, and the in vitro corrosion experiments were analyzed. The ionic concentrations of the human blood plasma and SBF (Ref 30) are presented in Table 2. Each substrate was immersed in 500 mL of SBF at pH 7.4 at 37 °C, respectively. After immersion in the SBF for 168 h, the substrates were removed from the SBF, thoroughly rinsed and gently washed well with distilled water and dried. The dried substrates were used for further characterization studies.

The SBF solution was prepared by the procedure developed by Kokubo and Takadama (Ref 31), and its composition is provided in Table 3. The SBF solution was replenished during the in vitro assessment to maintain the ionic concentration of the solution for every 24 h for all the experiments. The substrates after being chemically treated (labeled as HT) and after being immersed in SBF (labeled as HTI) were subjected to corrosion experiments in the SBF medium. Substrates without any chemical or surface treatment (labeled as UT) were used as controls for the comparison.

Table 1 Chemical compositions of the AZ91D and AZ31 alloys in wt.%

Alloys	Main Alloying elements, wt.%								
	Al	Zn	Mn	Si	Cu	Fe	Ca	Ni	Mg
AZ91D	9.20	0.71	0.30	0.03	0.01	0.003	…	…	Bal.
AZ31	2.83	0.8	0.37	…	0.002	…	…	…	Bal.

Table 2 Ionic concentrations of the SBF and the inorganic part of the human blood plasma (mmol⁻¹)

Ions	Na^+	K^+	Mg^{2+}	Ca^{2+}	Cl^-	HCO_3^-	HPO_4^-	SO_4^{2-}	pH
Plasma	142.0	3.6-5.5	1.0	2.12-2.6	95-107	27.0	0.65-1.45	1.0	7.3-7.4
SBF	142.0	5.0	1.0	2.5	131.0	5.0	1.0	1.0	7.4

Table 3 Chemical composition of the simulated body fluid (SBF) solution

S. no.	Reagents used	Grams in 1000 mL
1	NaCl	8.035
2	$NaHCO_3$	0.355
3	KCl	0.225
4	$K_2HPO_4 \cdot 3H_2O$	0.231
5	$MgCl_2 \cdot H_2O$	0.311
6	1 M HCl	40 mL
7	$CaCl_2$	0.292
8	Na_2SO_4	0.072
9	$((CH_2OH)_3CNH_2)$	6.118
10	1 M HCl	Appropriate amount for adjusting the pH 7.4

2.4 Surface Characterization of the Coatings

The surfaces of the untreated and treated Mg substrates before and after immersion in SBF were examined. XRD studies were performed using a RINT 2500 with a scattering angle of $20° \leq 2\theta \leq 80°$ and at a 2θ step of 0.02°. The structure and functional groups on the substrates were characterized using an IR spectrometer (Thermo Scientific, with a universal ATR attachment, range of 500-4000 cm⁻¹). The surface morphological behavior of the substrates was analyzed via SEM studies (JEOL, JSM-6360). The surface chemical analysis of the substrates was performed using energy-dispersive x-ray spectroscopy (EDS). The surface topography of the substrates was analyzed using an AFM (Agilent 5500 AFM, USA) instrument with Au-coated silicon cantilevers in non-contact mode with a resonance frequency of 26 kHz at a spring constant of 1.6 N/m under ambient atmosphere at room temperature. Contact angles of the substrates were measured using contact angle goniometry with an attention optical goniometer interfaced with image capture software by dropping 2 μL of liquid drops on the surface of the substrates.

2.5 Electrochemical Characterization of the Coatings

An electrochemical workstation (IVIUM Potentiostat/Galvanostat) with a three-electrode cell assembly was used for the electrochemical experiments. The substrates (AZ91D and AZ31 alloys) served as the working electrode with an exposure of the surface area of 1 cm² and a platinum foil as the counter electrode with a saturated calomel electrode (SCE) as the reference electrode. Corrosion experiments were conducted using SBF as the electrolyte solution. A stabilization period of 30 min was allowed to attain a stable value for the open circuit potential (OCP) prior to all the electrochemical measurements. Electrochemical impedance spectroscopy (EIS) measurements were performed with the scan frequency ranging from 10^5 to 10^{-1} Hz and with an amplitude voltage of 10 mV peak to peak using the AC signal with the OCP. Potentiodynamic polarization curves (PDP) were measured in the Tafel potential range of $\pm$ 250 mV from the OCP with a scan rate of 1 mVs⁻¹. To obtain reliable results, at least three parallel substrates were tested to verify the repeatability.

3. Results and Discussion

### 3.1 XRD Analysis of the DCPD Formation

Figure 1 shows the XRD patterns of the UT, HT, and HTI AZ91D and AZ31 alloys. Very intense peaks were observed for the Mg substrates. XRD peaks shown at 2θ values of 29.5°, 34.6°, 37°, 48.2°, 58°, 63.5°, 69° and 73° were attributed to the planes of (141), (002), (101), (102), (110), (103), (201) and (004) and are in good agreement with JCPDS 11-293, JCPDS 20-0669 and JCPDS-70-1433 (Ref 32). The XRD peaks at $2\theta = 29.5°$, 34.6°, 37° and 48.2° were identified as DCPD or brushite (JCPDS 11-293), whereas the peaks at $2\theta = 58°$, 63.5°, 69° and 73° corresponded to Mg, $Mg(OH)_2$ and MgO phase formation on the substrates after the immersion in SBF (Ref 33). No other calcium phosphate phases were found on the substrates. A thick coating formation has caused a lack of detection of magnesium peaks for the HT and HTI substrates.

Jiang et al. (Ref 34) investigated the formation of FHA coating on a biodegradable Mg-Zn-Zr alloy using two-step chemical treatment method using $Ca(NO_3) \cdot 4H_2O$ and $NH_4H_2PO_4$. According to their results, Mg-Zn-Zr alloys were treated with and without HF after chemical deposition for 2 h in a Ca-P solution. The Mg-Zn-Zr surface without HF treatment showed obvious HA diffraction peaks, indicating that the sheet material formed on the surface was hydroxyapatite. Jamesh et al. (Ref 35) studied the electrodeposition of HA coating on magnesium using $Ca(NO_3)_2$, $(NH_4)_3PO_4$ and NaOH. The XRD pattern results showed the conversion of DCPD to HA and that the intensity of HA was less when compared to DCPD. This was due to the reduction in the thickness of the DCPD coating during the alkali treatment. A portion of the DCPD coating dissolved by releasing Ca^{2+} and PO_4^{3-} ions.

Similarly, the intensities of the XRD peaks have decreased for the HT and HTI AZ91D and AZ31 surfaces, which may be associated with the thickness of the newly formed layer on the substrates. The formation of the new layer can be ascribed to a crystalline formation of DCPD or brushite coating on the surface of the AZ91D and AZ31 alloys. This DCPD coating can induce the nucleation and growth of CaP on Mg surfaces after immersion in SBF.

By using Scherer's equation (Ref 32), the average crystallite size was calculated for the surface-treated AZ91D and AZ31 substrates using the following formula:

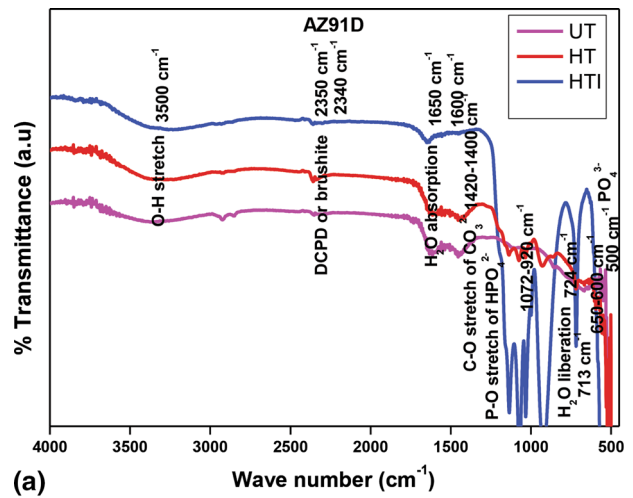$$D_{hkl} = \frac{k\lambda}{\beta \cos \theta}, \tag{Eq 1}$$
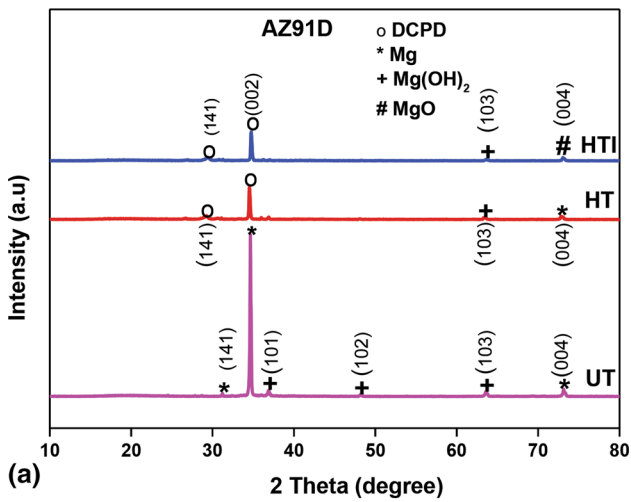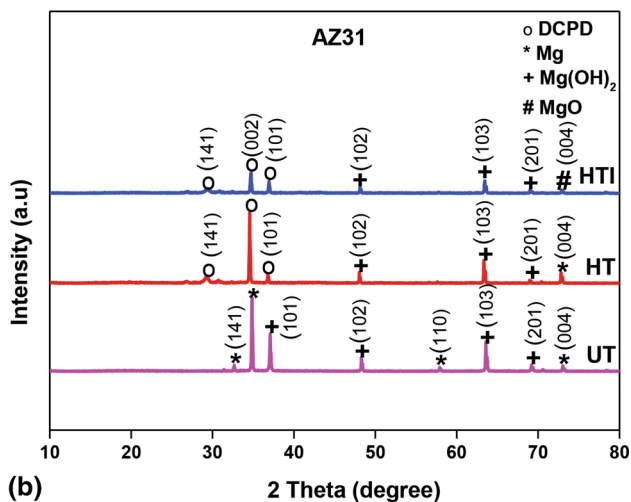
Fig. 1 X-ray diffraction patterns of the (a) AZ91D and (b) AZ31 alloys

Fig. 2 ATR-IR spectra of the (a) AZ91D and (b) AZ31 alloys

where k represents a constant (with a shape factor of 0.89), λ is the wavelength of the x-rays (0.154056 nm), β denotes the difference in the half-maximum width of the peaks obtained for the pure diffraction profile (in radians), θ is the diffraction angle and D_{hkl} represents the average diameter of the crystallites. The values obtained ranged from 40 to 80 nm, which is within the range of values reported by Wen et al. (Ref 17).
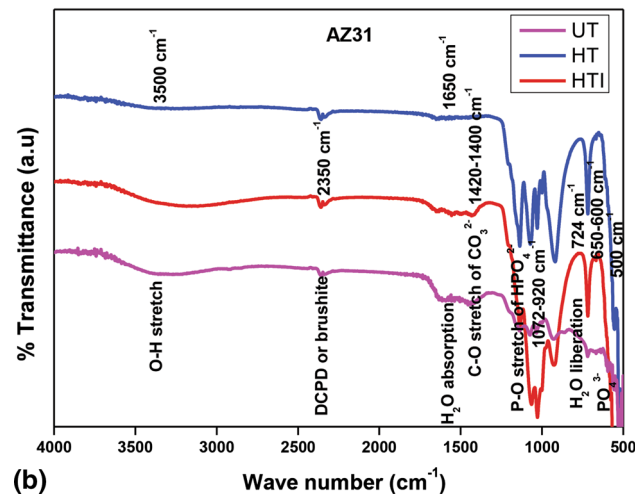
3.2 ATR-IR Spectroscopic Analysis of DCPD Formation

ATR-IR spectroscopic analysis was performed to identify the functional groups and vibration modes for each peak associated with the DCPD or brushite coating on the substrates. The ATR-IR spectra for the UT, HT, and HTI AZ91D and AZ31 alloys are presented in Fig. 2.

The absorption spectral bands at 3500 cm^{-1} correspond to O-H stretching, and the bending vibration modes between 1650 and 1600 cm^{-1} are assigned to H_2O absorption on the surface of the substrates. The absorption spectral bands detected between 2350 and 2340 cm^{-1} represent the formation of DCPD or brushite (Ref 33, 36, 37). The main absorption bands located at 1420-1400 cm^{-1} were attributed to the C-O stretch-

ing of the CO_3^{2-} group. The absorption spectral bands detected from 1072 to 920 cm^{-1} represent the existence of P-O stretching of the HPO_4^{2-} group. Bands at 724 and 713 cm^{-1} correspond to absorption of H_2O liberation. These observations are in close agreement with Xu et al. (Ref 38). The spectral bands at 650-600 cm^{-1} were assigned to triple (v_4) and double (v_2) degeneration of bending vibrational modes of O-P-O bonds of the phosphate group (Ref 30). The absorption bands at 560-500 cm^{-1} are due to the characteristic peak of the PO_4^{3-} group. A more detailed analysis allows the deduction of the presence of a carbonated component, where carbonate ions are substituted at A and B sites (Ref 35). The presence of CO_3^{2-}, HPO_4^{2-} and PO_4^{3-} bands in the entire spectrum confirms CaP layer formation over the Mg surfaces after immersion in SBF. The CaP nuclei could spontaneously grow once formed by consuming more Ca and P ions from the SBF. Hence, the ATR-IR spectrum confirms DCPD or brushite formation for the AZ91D and AZ31 alloys as evidenced by the XRD characterization (Ref 32, 37).

3.3 SEM and EDS Analysis of the DCPD Coating Formation

The surface morphological features of the as-deposited DCPD or brushite coatings on the substrates were examined using SEM. The elemental compositional analysis of the

coatings was investigated using EDS. The surface morphologies of the UT, HT AZ91D and AZ31 alloys are presented in Fig. 3(a), (b), (c), (d), (e) and (f). The micrograph of the UT surfaces (Fig. 3a and d) revealed a smooth uniform surface texture with unidirectional grooves representing the mechanically polished surface. The morphological features of the HT AZ91D surface reveal a denser flake-like DCPD crystal structure (Fig. 3b), and the clustering and dissolution of CaP flakes toward the periphery with irregular flakes of different dimensions over the entire surface were observed. Wang et al. (Ref 33) have studied Mg substrates with Ca and P ions solution containing $Ca(NO_3)_2$ and Na_2HPO_4 to create a DCPD surface layer. The

DCPD layer was effective in providing protection for the Mg substrate after 21 days of immersion in the SBF. Xu et al. (Ref 39) have investigated Mg-Mn-Zn alloy in an alkaline solution for the formation of a brushite ($CaHPO_4 \cdot 2H_2O$) surface coating. The results revealed that the DCPD coating was able to improve the surface biocompatibility of the Mg substrate since the DCPD coating transformed into an HAP phase with time. Additionally, during this transformation, acidic phosphate ions were released into solution, which have a neutralizing effect on the alkalization process. Furthermore, the surface treatment enhanced the bioactivity of the Mg-Mn-Zn alloy, which promoted bone formation and was also examined by Xu et al. (Ref 40).
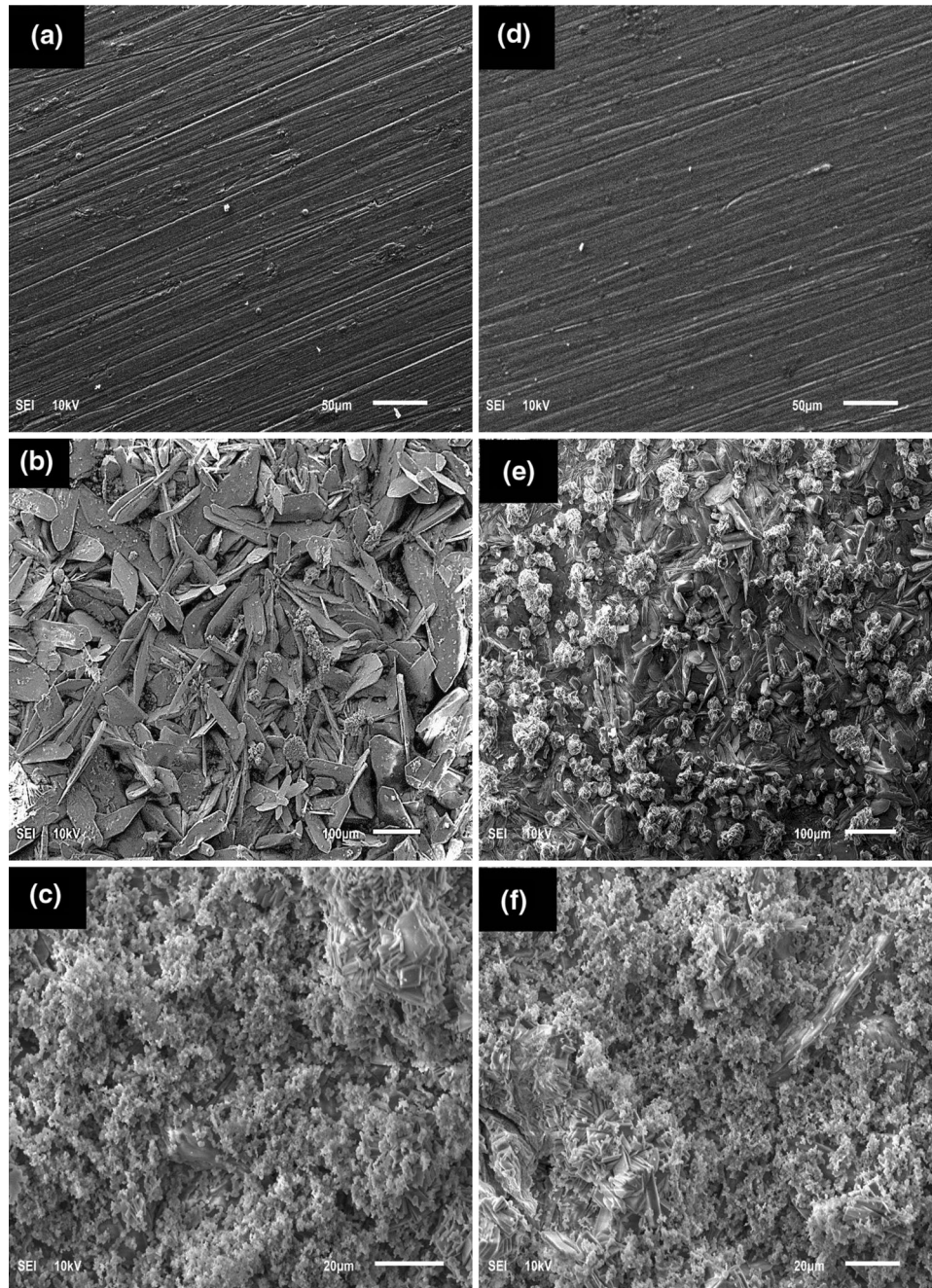

Fig. 3 SEM micrographs of AZ91D (a) UT, (b) HT and (c) HTI and SEM micrographs of AZ31 (d) UT, (e) HT and (f) HTI

Meanwhile, the HT AZ31 surface exhibited a cluster of spherical particles loosely covering the surface with the particles composed of radially oriented flake-like aggregates with different sized lengths were identified (Ref 33, 37). Yanovska et al. (Ref 41) have investigated the influence of low magnetic fields during a one-step dipping technique over Mg substrate with a solution containing $Ca(NO_3)_2 \cdot 4H_2O$ and $Na_2HPO_4 \cdot 12H_2O$. Depositions of both DCPD and HAP phases under the influence of the magnetic fields lead to the formation of a crystal orientation. Jamesh et al. (Ref 35) used an electrodeposition technique to produce three types of coatings, including DCPD, HAP and fluorapatite (FHA). The results showed that the FHA coating had long-term stability even after 1 month of immersion in a simulated body fluid.

For biomedical applications, particularly for bioimplants, the essential key requirement for successful osseointegration is the internal fixation of bone plates. Hence, these bone plates should have an essential CaP-forming ability over the surfaces for better fixation. In vitro evaluation tests have been performed to achieve this goal and typically carried out in SBF solution via immersion tests by immersing for a period of few weeks (Ref 42). After 168 h of immersion in an SBF solution, the morphology and elemental composition of HTI AZ91D and AZ31 alloys exhibited variations in their material surfaces exhibited by their significant behavior and the interaction of the ions present in the SBF solution. Additionally, the surfaces of the HTI AZ91D and AZ31 alloys showed a cluster of white particle formation uniformly over the entire surface area (Fig. 3c and f) due to the interaction of Ca and P ions adsorbed on the surfaces (Ref 33, 37) which was also evident from the ATR-IR and EDS analyses.

The EDS analysis was performed on the coated regions of the AZ91D and AZ31 alloys as depicted in Fig. 4. The spectrum reveals the presence of O, Ca, P, Cl, Na and Mg elements. The relative intensities of the Ca and P peaks have decreased for the HTI AZ91D and HTI AZ31 alloys (Fig. 4b and d) after immersion in the SBF solution, suggesting that Ca^{2+} and PO_4^{3-} ions diffused to the surface. Additionally, the CO_3^{2-} substituted for the PO_4^{3-} or OH^- and Mg^{2+}, Na^+ ions substituted for the Ca^{2+} position represent an apatite or CaP composition similar to human bone. The CaP ratio of the HT surfaces was found to be 0.82, and for the HTI surfaces, it was 1.58. However, both the values were lower than the theoretical value of HA (1.67). Hence, the formed DCPD coating was identified to be Ca-deficient HA (CDHA) (Ref 17). Dorozhkin (Ref 43) determined that the CDHA in the range of 1.33 and 1.55 for the Ca/P atomic ratio induced the formation of new bone in vivo. Hence, this confirms that the coating formed is DCPD or brushite.

3.4 AFM Analysis of the Coating Formation

The surface topography of the typical AFM images obtained for the UT, HT, and HTI AZ91D and AZ31 alloys is shown in Fig. 5. The surface topography of the UT surfaces (Fig. 5a and d) exhibited a relatively smooth surface texture along with few micro-scratches acquired during the mechanical polish. The HT surfaces acquired a nonuniform surface with the formation of pores (Fig. 5b and e) due to the roughness in the level of the microscale range during the deposition of the DCPD coating.

The arithmetic average roughness (R_a) obtained for the UT, HT, and HTI AZ91D and AZ31 alloys is shown in Table 4.
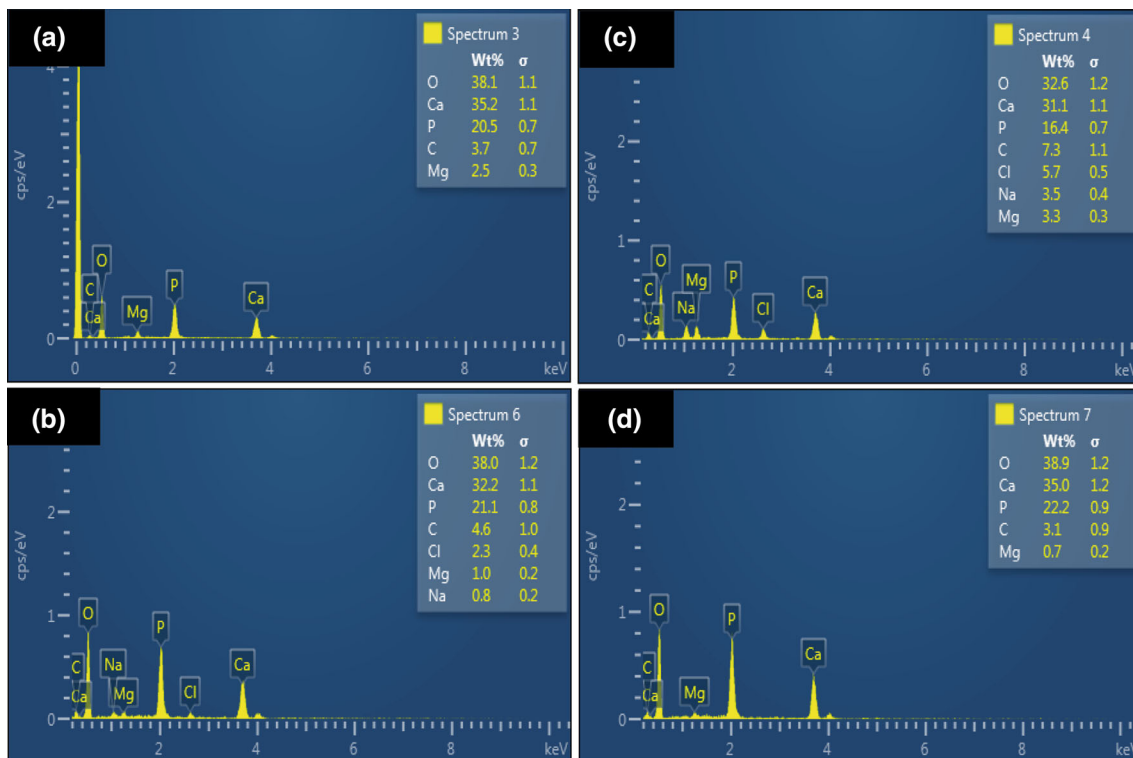

Fig. 4 EDS micrographs of AZ91D (a) HT and (b) HTI and EDS micrographs of AZ31 (c) HT and (d) HTI

$R_a - 0.65$ (a)

$R_a - 0.52$ (d)

$R_a - 1.23$ (b)

$R_a - 0.95$ (e)

$R_a - 0.92$ (c)
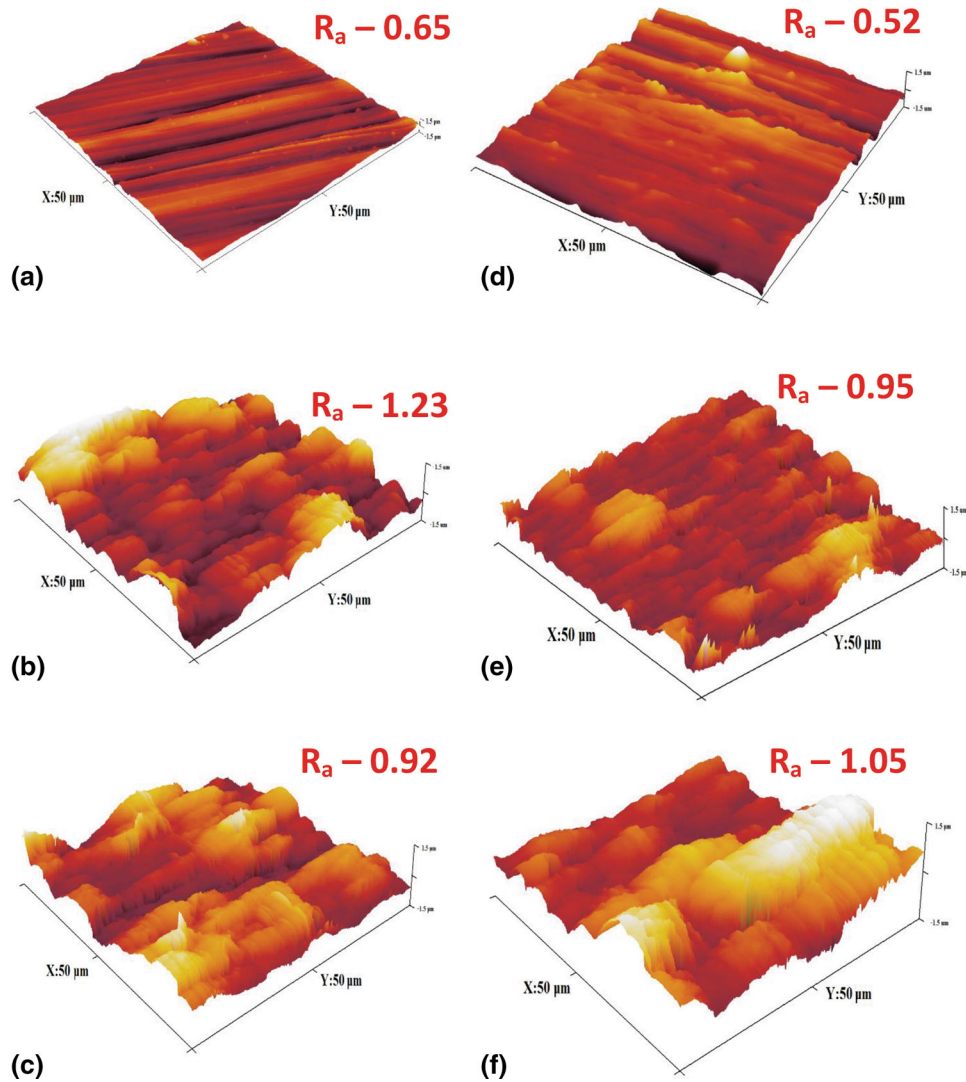
$R_a - 1.05$ (f)

Fig. 5 AFM micrographs of AZ91D (a) UT, (b) HT and (c) HTI and AFM micrographs of AZ31 (d) UT, (e) HT and (f) HTI

Table 4 Surface roughness values for the AZ91D and AZ31 alloys

Alloys	Surface treatment	Surface roughness R_a, μm
AZ91D	UT	− 0.65
	HT	− 1.23
	HTI	− 0.92
AZ31	UT	− 0.52
	HT	− 0.95
	HTI	− 1.05

Eventually, the surface roughness in the microscale range indicated that the roughness has increased for the HT surfaces compared with UT. The HTI surfaces (Fig. 5c and f) showed a slight increase in the surface roughness (R_a) values compared with the HT and UT AZ91D and AZ31 surfaces, indicating the formation of uneven pores with DCPD coating formation after immersion in the SBF solution. The increase in the roughness values was better because it increased the surface area and

provided more anchoring points for tissues, thus promoting tissue growth (Ref 37, 44, 45).

3.5 Contact Angle Measurements of the DCPD Coating on the Mg Alloys

The surface hydrophilicity of the Mg surfaces was examined using water contact angle (CA) measurements. The contact angle values for the UT, HT, and HTI AZ91D and AZ31 alloys are shown in Fig. 6. The CA was measured by dropping 2 μL of water droplets on the HT, HTI and UT surfaces at room temperature. The AZ91D and AZ31 alloys exhibited a relative hydrophilicity with water contact angles of 75.20° for UT AZ91D and 68.55° for UT AZ31. After DCPD treatment, the CA was reduced to 25.35° for HT AZ91D and to 38.80° for HT AZ31, indicating that the hydrophilicity was obviously enhanced. As from the ATR-IR analyses, more hydrophilic hydroxyl groups were introduced on the surfaces after DCPD treatment, which significantly enhanced the surface hydrophilicity. In contrast, compared with the UT alloys, the CA values for the HT AZ91D and AZ31 alloys decreased. They were further decreased to 18.35° and 24.20° for the HTI AZ91D and AZ31 alloys, respectively. Hence, the DCPD
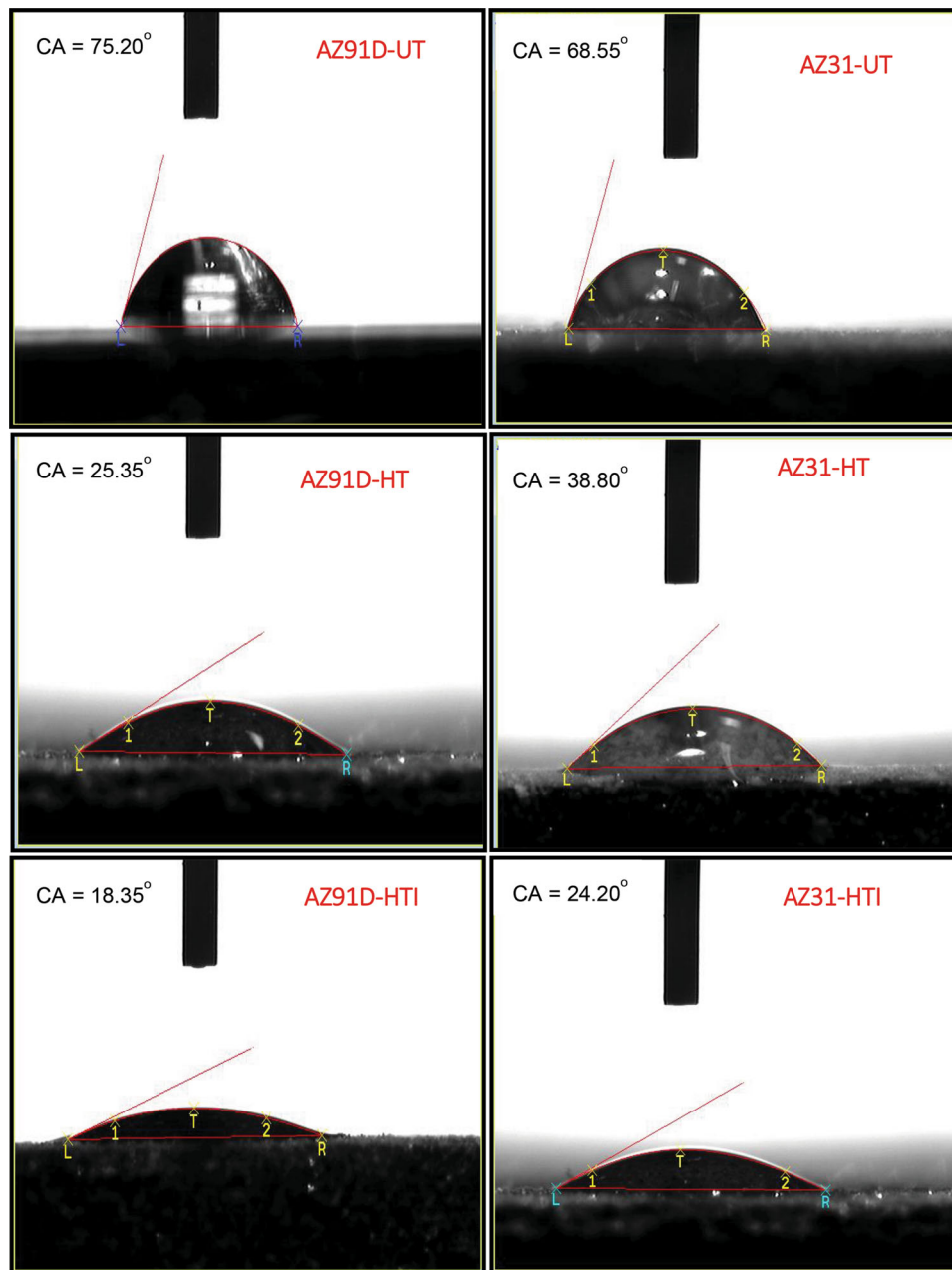
Fig. 6 Contact angle measurements for the AZ91D and AZ31 alloys

treatment after immersion in the SBF (HTI surfaces) has contributed to the improved and good hydrophilicity of the coatings (Ref 46–48).

3.6 Corrosion Behavior of the DCPD Coating

Electrochemical tests in the SBF were performed for the UT, HT, and HTI AZ91D and AZ31 alloys to assess the biocorrosion resistance properties of the Mg surfaces. The representative PDP plots are presented in Fig. 7. From the PDP curves, the corrosion potential (E_{corr}) values for all the substrates ranged from -1.36 to -1.52 V. Compared with the UT AZ91D substrate (-1.4532 V), the corrosion potential values observed for the HT and HTI AZ91D substrates were -1.3859 and -1.3609 V, respectively. Similarly, the corrosion potential value for the UT AZ31 substrate was 1.5221 V, and for the HT and HTI AZ31 substrates, it was -1.5002 and -1.4855 V, respectively.

The E_{corr} values shifted toward the nobler direction after immersion in the SBF for the HTI AZ91D and AZ31 alloys, corresponding to a higher resistance to corrosion initiation in the SBF. The corrosion current density (i_{corr}) value observed for AZ91D was significantly decreased from 17.45 to 1.46 μA/cm^2. Meanwhile, for AZ31, the current density value decreased from 12.34 to 3.77 μA/cm^2. Obviously, the i_{corr} value was two orders of magnitude with a lower corrosion rate of 33.48 mpy for HTI AZ91D compared with the UT, HT AZ91D and AZ31 substrates. Xu et al. (Ref 39) studied Mg-Mn-Zn alloy in alkaline solution to form a brushite ($CaHPO_4 \cdot 2H_2O$) coating on its surface. The results showed that the layer formed was porous and did not prevent corrosion in a simulated body fluid. Additionally, the degradation rate was significantly reduced

with reasonable protection against the corrosive effects of the simulated body fluid. Yanovska et al. (Ref 41) observed that dipping Mg substrates into an aqueous solution containing $Ca(NO_3)_2 \cdot 4H_2O$ and $Na_2HPO_4 \cdot 12H_2O$ to deposit both DCPD and HAP phases has provided coatings with enhanced corrosion resistance, which in turn reduced their degradation rate.

The electrochemical process can be studied via the electrochemical reactions that take place between the solution interface and electrode by varying the corrosion potential with respect to the immersion time. Since the anodic and cathodic

branches were asymmetrical, the E_{corr} and i_{corr} values were extracted using Tafel extrapolation from the cathodic polarization curves. Tafel regions utilized for the polarization curve assessment start at approximately 50 mV (generally up to 100 mV) from the E_{corr}, and the open circuit potential is in the steady state in the cathodic and in the anodic branches of the polarization curve. However, for many metals and alloys showing active–passive behavior, the anodic branch of the polarization curve should not be used to assess material performance because of the absence of a linear Tafel region (Ref 49–51). During Tafel analyses, the cathodic polarization branch was only utilized for the calculation of i_{corr}. The anodic branch was not considered due to the abnormal behavior (negative difference effect: the increase in the rate of hydrogen evolution with the increase in the anodic polarization) exhibited by the Mg alloys during anodic dissolution (Ref 52-55). To calculate i_{corr}, a slope was drawn in the cathodic branch at
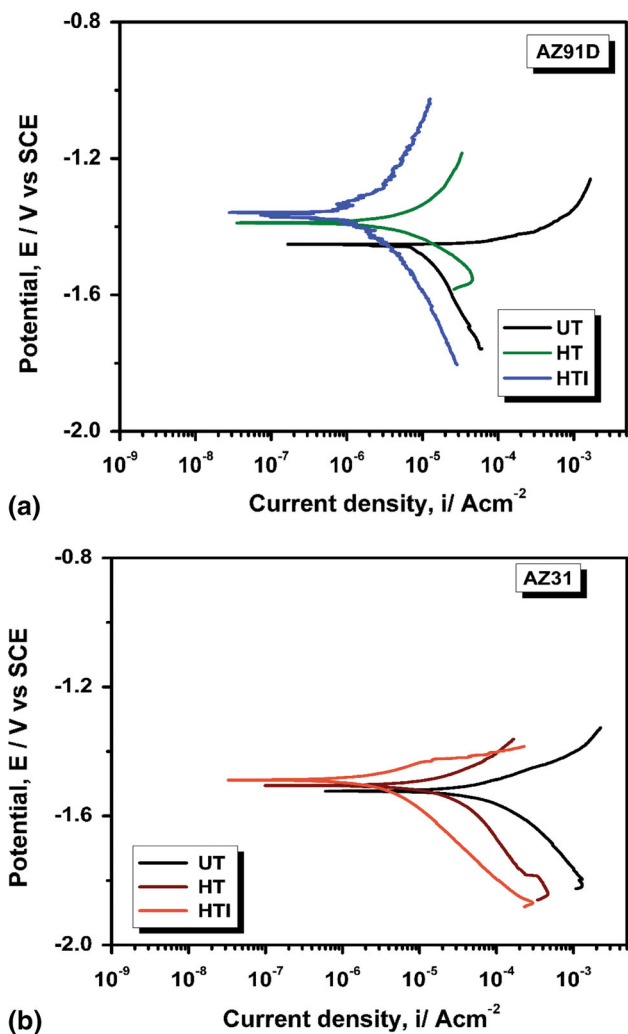

Fig. 7 Potentiodynamic polarization curves for the (a) AZ91D and (b) AZ31 alloys in the SBF solution
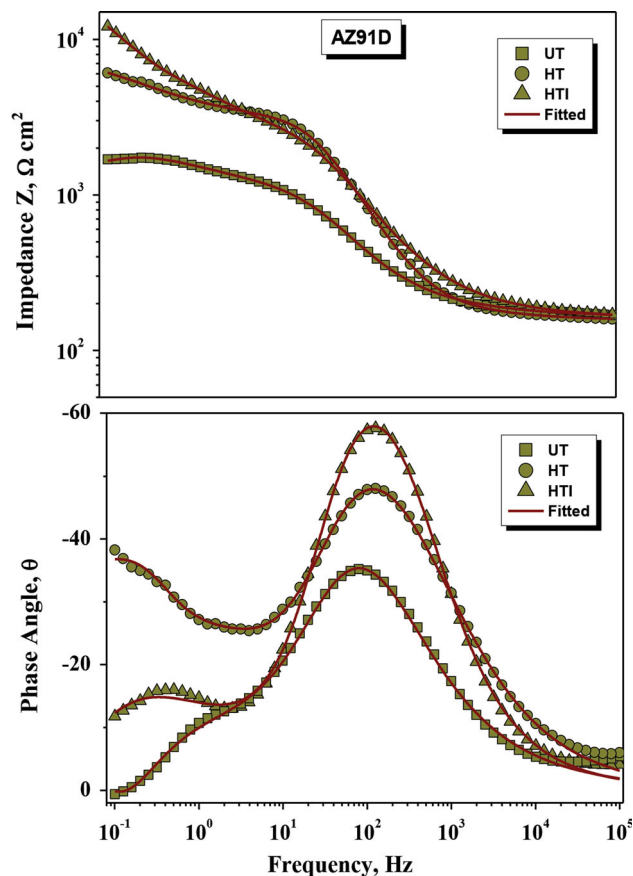

Fig. 8 Bode impedance and bode phase angle plots for the AZ91D alloy in the SBF solution

Table 5 Tafel polarization parameters for the AZ91D and AZ31Mg alloys in the SBF solution

Alloys	Surface treatment	E_{corr}, V	i_{corr}, µA cm^2	β_a mV/decade	β_c mV/decade	R_p, kΩ cm^2	Corrosion rate, mm/year
AZ91D	UT	− 1.4532	17.4591	87	98	1.146	0.398
	HT	− 1.3859	5.8862	69	84	2.794	0.134
	HTI	− 1.3609	1.4656	75	92	12.241	0.033
AZ31	UT	− 1.5221	12.3439	69	81	1.310	0.282
	HT	− 1.5002	16.3740	112	93	1.347	0.374
	HTI	− 1.4855	3.7713	102	87	5.405	0.086

− 100 mV from the meeting point of the anodic and cathodic curves (E_{corr}) in the Tafel plot. The corrosion current of the point at which the slope line intersected with the horizontal line drawn from the E_{corr} was considered to be i_{corr} (Ref [41]). The various parameters, viz. corrosion potential (E_{corr}), corrosion current density (i_{corr}), polarization resistance (R_p) and the corrosion rate (C_{Ri}) of the substrates, were calculated, and the values are provided in Table 5. The instantaneous corrosion rate (mm/year) was calculated by using the following formula (Ref [32]):

$$C_{Ri} = 22.85_{i_{corr}} \tag{Eq 2}$$

where C_{Ri} is the corrosion rate and i_{corr} is the corrosion current density of the AZ91D and AZ31 alloys.

When magnesium alloys are exposed to the corrosion environment medium, the penetration of the electrolyte along with the chemical dissolution results in spontaneous corrosion in the form of corrosion products over the entire surface. This results in an increase in corrosion potential due to the protection of the corrosion product layer and a decrease in the active region, which becomes enhanced with a prolonged exposure times. Hence, it is very difficult for corrosion products to precipitate in the cathode region where the process of hydrogen evolution occurs. The corrosion products mainly precipitate at the vicinity of the anodic region due to the diffusion of OH⁻ ions (Ref [47]). Chloride ions present in the SBF solution transform the MgO/Mg(OH₂) film surface into soluble MgCl₂ in addition to corrosion products. Due to the Mg(OH₂) dissolution, the surface will be more active, and the decrease in the protected area will promote further dissolution of Mg. As manifested by a constant potential, an equilibrium exists between the dissolution and formation of the established corrosion products that are sufficiently immersed for a longer time. Due to the prolonged immersion time, the corrosion potential moves toward a nobler direction. As it is known, during immersion in an SBF, electrolytes gradually penetrate into the coating (Ref [44, 46, 47, 56]). Hence, the polarization results suggested that the HTI AZ91D was significantly improved with a better corrosion resistance after DCPD formation on the surfaces, which is essential for long-term implants.

EIS is a powerful tool that can be used to analyze the corrosion of coated metals and alloys. EIS provides information about the quantitative evaluation and its corrosion properties of a system. It is very difficult to use this technique in conventional electrochemical measurements. Detailed information on the corrosion process that occurs at the electrolyte/electrode interface can be evaluated using an appropriate equivalent circuit model with EIS data interpretation. Representative EIS curves obtained for the Mg alloys in SBF were evaluated as a function of immersion time (Ref [44, 46, 47]).

The impedance response of the UT, HT and HTI AZ91D and AZ31 alloys was assessed, and the representative bode phase angles and bode impedance plots are provided in Fig. 8. The electrochemical impedance response for the UT AZ91D showed a single spectrum, representing a thin passive oxide film on the surface. The HT and HTI AZ91D represent the entire spectrum with two time constants and a well-separated range in the frequency domain, one at the higher frequency and one at the lower frequency regions with the phase angle approaching approximately 45° and 60° in the intermediate frequency regions, which corresponds to the formation of a
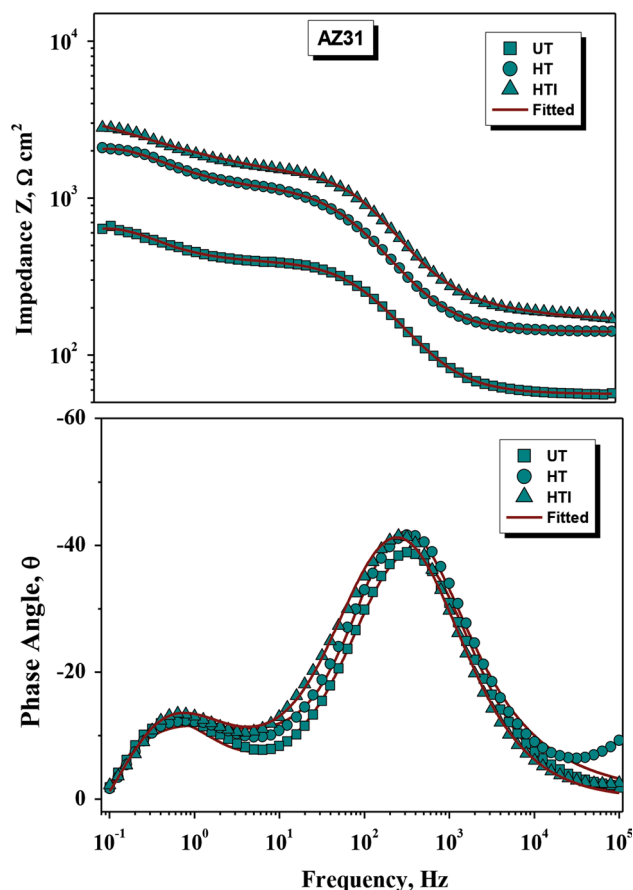

Fig. 9 Bode impedance and bode phase angle plots for the AZ31 alloy in the SBF solution

passive film on the metal surface. The secondary region begins at an intermediate frequency, and the attained phase angle values were approximately 30° and 20° in the lower frequency regions, which corresponds to the formation of the DCPD layer as confirmed by the XRD and ATR-IR analyses (Ref [30]). However, a small bump observed for HTI AZ91D in the lower frequency region from 10^0 to 10^{-1} Hz may be due to the formation of Mg(OH)₂ layer. The chloride ions from the SBF solution can transform the Mg(OH₂) film surface into soluble MgCl₂ in addition to corrosion products. Thus, the surface can be more active due to the dissolution of Mg(OH₂), and there was a decrease in the protective surface area to promote further dissolution of Mg (Ref [47]).

The impedance response for the UT, HT and HTI AZ31 alloys was examined, and the bode phase angles and bode impedance plots are depicted in Fig. 9. All the spectra exhibited similar shapes with the presence of two time constants and were similar to AZ91D. The impedance response behavior of HTI AZ31 was significantly improved with the high corrosion resistance compared with the HT and UT AZ31 substrates. Wang et al. (Ref [33]) have also investigated similar observations in research studies on the improvement in corrosion resistance of magnesium in simulated body fluid via DCPD coating. Their studies revealed that DCPD coating composed of bar-shaped crystals was deposited on the surface of magnesium to slow down the corrosion rate of the substrates. The DCPD-coated substrates were evaluated in a simulated body fluid (SBF) with uncoated substrates as a control, and the corresponding SBF

was analyzed at various time periods of 3, 5, 7, 14 and 21 days of immersion. The results reveal that after 3 days of immersion in the SBF, the DCPD coating was still intact and completely covered the substrate. DCPD dissolution was observed on the 3rd day and became noticeable for 5th and 7th day, and it was found that there was no new phase formation for the entire immersion period.

To analyze the capacitive behavior of an electrochemical system, instead of using a capacitor (C), a constant phase element (CPE) was introduced for the compensation of the nonhomogeneity at the surface of the electrode. The impedance behavior for a constant phase element is given by

$$Z_{CPE} = [Q(j\omega)n]^{-1}, \qquad (Eq\ 3)$$

where Z is the impedance, Q is CPE, j denotes an imaginary number ($j = \sqrt{1}$), ω is the angular frequency $= 2\sqrt{\Pi}f$ (rad s^{-1}) and Q and n denote the frequency-independent parameters that mainly depend on the temperature. The condition for any electrochemical system is that n is $-1 \leq n \leq 1$. CPE (Q) denotes an ideal capacitor when $n = 1$, an ideal resistor when $n = 0$ and a pure inductor when $n = -1$.

An equivalent circuit model fitted for the AZ91D and AZ31 alloys was $R_s(R_{ct}Q_{dl})$ (R_fQ_f), and the circuit diagrams are presented in Fig. 10. The proposed model used to fit the spectra
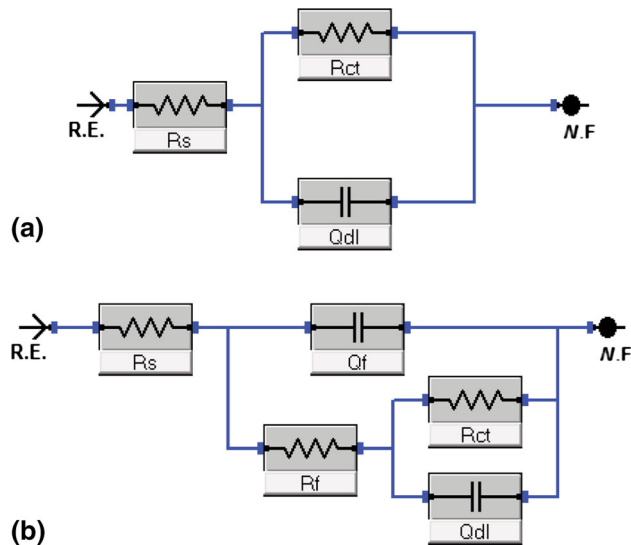
for the UT substrates was $R_s(R_{ct}Q_{dl})$ (Fig. 10a), and for the HT and HTI substrates, it was $R_s(R_{ct}Q_{dl})$ (R_fQ_f) (Fig. 10b). In this case, Q_{dl} and Q_f were assigned to the capacitance of the coating layer and the oxide layer formed at the surface of the AZ91D and AZ31 alloys. R_s represents the solution resistance, whereas the R_{ct} and R_f parameters correspond to the charge transfer resistance of the coating layer and the oxide layer, respectively. The main criteria for choosing the best model to fit and interpret the EIS data are a low% error in the parameters and low Chi-square values.

The electrochemical impedance parameters were obtained from the impedance spectra, and the fitted values are provided in Table 6. Table 6 shows that the charge transfer resistance value of the barrier oxide layer (R_f) initially increased because of the insulating nature of the oxide film that formed and aged with the SBF solution. Meanwhile, for the HT and HTI AZ91D and AZ31 alloys, the resistance values increased for the coating layer (R_{ct}), which may be due to the solution ion adsorption on the coating layer (Ref 32). However, the HTI AZ91D had a higher corrosion resistance value compared with the other substrates due to the DCPD formation along with the adsorption of more CaP ions after 168 h of immersion in the SBF solution. When the magnesium alloys were exposed to the air environment, an Mg (OH)$_2$ layer formed on the metal surface, which is slightly soluble and reacts with chorine ions to form highly soluble magnesium chloride and hydrogen gas. Additionally, the oxide layer fully covers and seals the metal surface, which forms a kinetic barrier or passive layer that physically limits or prevents further migration of ionic species over the metal oxide/solution interface (Ref 44, 45, 57).

4. Conclusions

A biocompatible DCPD or brushite coating on the surface of AZ91D and AZ31 alloys was successfully fabricated. Surface treatment was performed using Ca(NO$_3$)·4H$_2$O and KH$_2$PO$_4$ followed by heat treatment to enhance the performance of the corrosion resistance and biocompatibility. This surface treatment method allows the surface with the formed DCPD layer to retard the deterioration of AZ91D and AZ31 alloys. The DCPD coating with the formation of a CaP layer was confirmed via XRD, ATR-IR, SEM, EDS and AFM studies. The superhydrophilic nature of the DCPD coatings was determined via the contact angle. The polarization and impedance results predicted that the HTI AZ91D exhibited a lower current density and a higher corrosion resistance compared with the other substrates and confirmed its higher bioresistivity due to the surface treatment followed by immersion in the SBF for 168 h. From

Fig. 10 Equivalent circuit diagrams fitted as $R_s(R_{ct}Q_{dl})$ and $R_s(R_{ct}Q_{dl})$ (R_fQ_f) for the AZ91D and AZ31 alloys: (a) UT and (b) HT, HTI (R_s—solution resistance, R_{ct}—charge transfer resistance, R_f—film resistance, Q_{dl}—CPE of the double-layer capacitance and Q_f—CPE of the film capacitance)

Table 6 Electrochemical impedance parameters for the AZ91D and AZ31Mg alloys in the SBF solution

Alloys	Surface treatment	R_s, Ω cm^2	R_{ct}, Ω cm^2	Q_{dl}, μF cm^{-2}	n	R_f, Ω cm^2	Q_f, μF cm^{-2}	n
AZ91D	UT	54.28	1665	74.52	0.90	…	…	…
	HT	48.57	6005	10.58	0.94	2404	23.57	0.93
	HTI	42.58	12,521	4.25	0.93	2921	18.04	0.92
AZ31	UT	62.01	631	79.24	0.89	…	…	…
	HT	58.21	2048	23.74	0.93	996	45.36	0.94
	HTI	49.65	2988	12.57	0.94	1454	32.54	0.92

this investigation, we determined that there was a considerable deterioration of the UT AZ91D and AZ31 alloys in the SBF, whereas the DCPD coating retarded the biodeterioration and favored the CaP layer formation on the surface of the AZ91D and AZ31 alloys. Among the surface-treated AZ91D and AZ31 alloys, DCPD treatment and immersion in the SBF for the HTI AZ91D were found to impart excellent bioactivity with a higher corrosion resistance compared with the AZ31 alloy. Hence, the present surface treatment is strongly proposed for attaining good biocompatibility, osteoconductivity and longevity of AZ91D and AZ31 alloys that serve as long-term orthopedic implants.

Acknowledgments

References

1. X. Gu, Y. Zheng, Y. Cheng, S. Zhong, and T. Xi, In Vitro Corrosion and Biocompatibility of Binary Magnesium Alloys, *Biomaterials*, 2009, **304**, p 484–498

2. A. Lambotte, L'utilisation du Magnesium Comme Materiel Perdu Dans L'osteosynthese, *Bull. Mem. Soc. Nat. Chir.*, 1932, **28**, p 1325–1334

3. G.L. Song and A. Atrens, Understanding Magnesium Corrosion—A Framework for Improved Alloy Performance, *Adv. Eng. Mater.*, 2003, **5**, p 837–858

4. C. Ying-liang, Q. Ting-wei, W. Hui-min, and Z. Zhao, Comparison of Corrosion Behaviors of AZ31, AZ91, AM60 and ZK60 Magnesium Alloys, *Trans. Nonferrous Met. Soc. China*, 2009, **19**, p 517–524

5. A. Abdal-hay, N.A.M. Barakat, and J.K. Lim, Hydroxyapatite-doped Poly(Lactic Acid) Porous Film Coating for Enhanced Bioactivity and Corrosion Behavior of AZ31Mg Alloy for Orthopedic Applications, *Ceram. Int.*, 2013, **39**, p 183–195

6. D. Sreekanth, N. Rameshbabu, and K. Venkateswarlu, Effect of Various Additives on Morphology and Corrosion Behavior of Ceramic Coatings Developed on AZ31 Magnesium Alloy by Plasma Electrolytic Oxidation, *Ceram. Int.*, 2012, **38**, p 4607–4615

7. S.V. Dorozhkin, Calcium Orthophosphate Coatings on Magnesium and Its Biodegradable Alloys, *Acta Biomater.*, 2014, **10**, p 2919–2934

8. S. Shadanbaz and G.J. Dias, Calcium Phosphate Coatings on Magnesium Alloys for Biomedical Applications: A Review, *Acta Biomater.*, 2012, **8**, p 20–30

9. R.A. Surmenev, M.A. Surmeneva, and A.A. Ivanova, Significance of Calcium Phosphate Coatings for the Enhancement of New Bone Osteogenesis—A Review, *Acta Biomater.*, 2014, **10**, p 557–579

10. S.R. Paital and N.B. Dahotre, Calcium Phosphate Coatings for Bio-implant Applications: Materials, Performance Factors, and Methodologies, *Mater. Sci. Eng. Rep.*, 2009, **66**, p 1–70

11. Y. Chen and X. Miao, Effect of Fluorine Addition on the Corrosion Resistance of Hydroxyapatite Ceramics, *Ceram. Int.*, 2004, **30**, p 1961–1965

12. M. Pan, X. Kong, Y. Cai, and J. Yao, Hydroxyapatite Coating on the Titanium Substrate Modulated by a Recombinant Collagen-Like Protein, *Mater. Chem. Phys.*, 2011, **126**, p 811–817

13. J.E. Gray Munro and M. Strong, The Mechanism of Deposition of Calcium Phosphate Coatings from Solution onto Magnesium Alloy AZ31, *J. Biomed. Mater. Res. A*, 2009, **90**, p 339–350

14. D. Gopi, P.R. Bhalaji, S. Ramya, and L. Kavitha, Evaluation of Biodegradability of Surface Treated AZ91 Magnesium Alloy in SBF Solution, *J. Ind. Eng. Chem.*, 2015, **23**, p 218–227

15. M. Tomozawa and S. Hiromoto, Microstructure of Hydroxyapatite- and Octacalcium Phosphate-Coatings Formed on Magnesium by a Hydrothermal Treatment at Various pH Values, *Acta Mater.*, 2011, **59**, p 355–363

16. J. Liang, B.G. Guo, J. Tian, H.W. Liu, J.F. Zhou, W.M. Liu, and T. Xu, Effects of NaAlO₂ on Structure and Corrosion Resistance of Microarc Oxidation Coatings Formed on AM60B Magnesium Alloy in Phosphate-KOH Electrolyte, *Surf. Coat. Technol.*, 2005, **199**, p 121–126

17. C. Wen, S. Guan, L. Peng, C. Ren, X. Wang, and Z. Hu, Characterization and Degradation Behavior of AZ31 Alloy Surface Modified by Bone-Like Hydroxyapatite for Implant Applications, *Appl. Surf. Sci.*, 2009, **255**, p 6433–6438

18. L. Li, J. Gao, and Y. Wang, Evaluation of Cyto-toxicity and Corrosion Behavior of Alkali-Heat-Treated Magnesium in Simulated Body Fluid, *Surf. Coat. Technol.*, 2004, **185**, p 92–98

19. Y. Zhu, G. Wu, Y. Hong Zhang, and Q. Zhao, Growth and Characterization of Mg(OH)₂ Film on Magnesium Alloy AZ31, *Appl. Surf. Sci.*, 2011, **257**, p 6129–6137

20. C. Lorenz, J.G. Brunner, P. Kollmannsberger, L. Jaafar, B. Fabry, and S. Virtanen, Effect of Surface Pre-treatments on Biocompatibility of Magnesium, *Acta Biomater.*, 2009, **5**, p 2783–2789

21. H. Zhao, S. Cai, S. Niu, R. Zhang, X. Wu, G. Xu, and Z. Ding, The Influence of Alkali Pretreatments of AZ31 Magnesium Alloys on Bonding of Bioglass-Ceramic Coatings and Corrosion Resistance for Biomedical Applications, *Ceram. Int.*, 2015, **41**, p 4590–4600

22. Y. Su, Y. Lu, Y. Su, J. Hu, J. Lian, and G. Li, Enhancing the Corrosion Resistance and Surface Bioactivity of a Calcium-Phosphate Coating on a Biodegradable AZ60 Magnesium Alloy via a Simple Fluorine Post-treatment Method, *RSC Adv.*, 2015, **5**, p 56001–56010

23. L. Zhang, S. Li, H. Li, and L. Pei, Bioactive Surface Modification of Carbon/Carbon Composites with Multilayer SiC-SiC Nanowire-Si Doped Hydroxyapatite Coating, *J. Alloys Compd.*, 2018, **740**, p 109–117

24. X. Zhao, X. Wang, H. Xin, L. Zhang, J. Yang, and G. Jiang, Controllable Preparation of SiC Coating Protecting Carbon Fiber from Oxidation Damage During Sintering Process and SiC Coated Carbon Fiber Reinforced Hydroxyapatite Composites, *Appl. Surf. Sci.*, 2018, **450**, p 265–273

25. L. Zhang, L. Pei, H. Li, S. Li, S. Liu, and Y. Guo, Preparation and Characterization of Na and F Co-Doped Hydroxyapatite Coating Reinforced by Carbon Nanotubes and SiC Nanoparticles, *Mater. Lett.*, 2018, **218**, p 161–164

26. Z. Leilei, L. Hejun, L. Kezhi, Z. Yulei, L. Shoujie, G. Qian, and L. Shaoxian, Micro-oxidation Treatment to Improve Bonding Strength of Sr and Na Co-substituted Hydroxyapatite Coatings for Carbon/Carbon Composites, *Appl. Surf. Sci.*, 2016, **378**, p 136–141

27. S. Liu, H. Li, L. Zhang, L. Feng, and P. Yao, Strontium and Magnesium Substituted Dicalcium Phosphate Dehydrate Coating for Carbon/Carbon Composites Prepared by Pulsed Electrodeposition, *Appl. Surf. Sci.*, 2015, **359**, p 288–292

28. Z. Leilei, L. Hejun, L. Kezhi, Z. Shouyang, F. Qiangang, Z. Yulei, L. Jinhua, and L. Wei, Preparation and Characterization of Carbon/SiC Nanowire/Na-Doped Carbonated Hydroxyapatite Multilayer Coating for Carbon/Carbon Composites, *Appl. Surf. Sci.*, 2014, **313**, p 85–92

29. L. Zhang, L. Pei, H. Li, and F. Zhu, Design and Fabrication of Pyrolytic Carbon-SiC-Fluoridated Hydroxyapatite-Hydroxyapatite Multilayered Coating on Carbon Fibers, *Appl. Surf. Sci.*, 2019, **473**, p 571–577

30. Y. Sasikumar and N. Rajendran, Influence of Surface Modification on the Apatite Formation and Corrosion Behavior of Ti and Ti-15Mo Alloy for Biomedical Applications, *Mater. Chem. Phys.*, 2013, **138**, p 114–123

31. T. Kokubo and H. Takadama, How Useful is SBF in Predicting In Vivo Bone Bioactivity, *Biomaterials*, 2006, **27**, p 2907–2915

32. Y. Sasikumar, M.M. Solomon, L.O. Olasunkanmi, and E.E. Ebenso, Effect of Surface Treatment on the Bioactivity and Electrochemical Behavior of Magnesium Alloys in Simulated Body Fluid, *Mater. Corros.*, 2017, **68**, p 776–790

33. Y. Wang, M. Wei, and J. Gao, Improve Corrosion Resistance of Magnesium in Simulated Body Fluid by Dicalcium Phosphate Dihydrate Coating, *Mater. Sci. Eng. C*, 2009, **29**, p 1311–1316

34. S.T. Jiang, J. Zhang, S.Z. Shun, and M.F. Chen, The Formation of FHA Coating on Biodegradable Mg-Zn-Zr Alloy using a Two-Step Chemical Treatment Method, *Appl. Surf. Sci.*, 2016, **388**, p 424–430

35. M. Jamesh, S. Kumar, and T.S.N. Sankara Narayanan, Electrodeposition of Hydroxyapatite Coating on Magnesium for Biomedical Applications, *J. Coat. Technol. Res.*, 2012, **9**, p 495–502

36. Y. Su, G. Li, and J.A. Lian, Chemical Conversion Hydroxyapatite Coating on AZ60 Magnesium Alloy and Its Electrochemical Corrosion Behaviour, *Int. J. Electrochem. Sci.*, 2012, **7**, p 11497–11511

37. B. Sridevi, J. Gérrard Eddy, and F. Derek, Growth of Flower-Like Brushite Structures on Magnesium Substrates and Their Subsequent Low Temperature Transformation to Hydroxyapatite, *Am. J. Biomed. Eng.*, 2014, **4**, p 79–87

38. J. Xu, I.S. Butler, and F.R.G. Denis, FT-Raman and High-Pressure Infrared Spectroscopic Studies of Dicalcium Phosphate Dihydrate ($CaHPO_4$ $2H_2O$) and Anhydrous Dicalcium Phosphate ($CaHPO_4$), *Spectrochim. Acta A*, 1999, **55**, p 2801–2809

39. L. Xu, E. Zhang, and K. Yang, Phosphating Treatment and Corrosion Properties of Mg-Mn-Zn Alloy for Biomedical Application, *J. Mater. Sci. Mater. Med.*, 2009, **20**, p 859–867

40. L. Xu, F. Pan, G. Yu, L. Yang, E. Zhang, and K. Yang, In Vitro and In Vivo Evaluation of the Surface Bioactivity of a Calcium Phosphate Coated Magnesium Alloy, *Biomaterials*, 2008, **30**, p 1512–1523

41. A. Yanovska, V. Kuznetsov, A. Stanislavov, S. Danilchenko, and L. Sukhodub, Calcium–Phosphate Coatings Obtained Biomimetically on Magnesium Substrates Under Low Magnetic Field, *Appl. Surf. Sci.*, 2012, **258**, p 8577–8584

42. L.L. Hench, Bioceramics, *J. Am. Ceram. Soc.*, 1998, **81**, p 1705–1728

43. S.V. Dorozhkin, A Review on the Dissolution Models of Calcium Apatites, *Prog. Cryst. Growth Charact.*, 2002, **44**, p 45–61

44. T.M. Mukhametkaliyev, M.A. Surmeneva, A. Vladescu, C.M. Cotruta, M. Braic, M. Dinu, M.D. Vranceanu, I. Pana, M. Muellere, and R.A. Surmenev, A Biodegradable AZ91 Magnesium Alloy Coated with a Thin Nanostructured Hydroxyapatite for Improving the Corrosion Resistance, *Mater. Sci. Eng. C*, 2017, **75**, p 95–103

45. A.M. Fekry and M.A. Ameer, Electrochemistry and Impedance Studies on Titanium and Magnesium Alloys in Ringer's Solution, *Int. J. Electrochem. Sci.*, 2011, **6**, p 1342–1354

46. C.J. Pan, L. Pang, Y. Hou, Y.B. Lin, T. Gong, T. Liu, W. Ye, and H.Y. Ding, Improving Corrosion Resistance and Biocompatibility of Magnesium Alloy by Sodium Hydroxide and Hydrofluoric Acid Treatments, *Appl. Sci.*, 2017, **7**, p 33

47. Y.J. Zhang, C.W. Yan, F.H. Wang, and W.F. Li, Electrochemical Behavior of Anodized Mg Alloy AZ91D in Chloride Containing Aqueous Solution, *Corros. Sci.*, 2005, **47**, p 2816–2831

48. R.G. Guan, I. Johnson, T. Cui, T. Zhao, Z.Y. Zhao, X. Li, and H. Liu, Electrodeposition of Hydroxyapatite Coating on Mg-4.0Zn-1.0Ca-0.6Zr Alloy and In Vitro Evaluation of Degradation, Hemolysis, and Cytotoxicity, *J. Biomed. Mater. Res. A*, 2012, **100A**, p 999–1015

49. M.G. Fontana, *Corrosion Engineering*, 3rd ed., McGraw-Hill, New York, 1986

50. E. Stansbury and R. Buchanan, *Fundamentals of Electrochemical Corrosion*, 1st ed., ASM International, Materials Park, 2000

51. G.L. Song, A. Atrens, D. St. John, X. Wu, and J. Nairn, The Anodic Dissolution of Magnesium in Chloride and Sulphate Solutions, *Corros. Sci.*, 1997, **39**, p 1981–2004

52. Y.R. Chu and C.S. Lin, Citrate Gel Conversion Coating on AZ31 Magnesium Alloys, *Corros. Sci.*, 2014, **87**, p 288–296

53. M.C. Zhao, P. Schmutz, S. Brunner, M. Liu, G.L. Song, and A. Atrens, An Exploratory Study of the Corrosion of Mg Alloys During Interrupted Salt Spray Testing, *Corros. Sci.*, 2009, **51**, p 1277–1292

54. T.R. Thomaz, C.R. Weber, T. Pelegrini, Jr., L.F.P. Dick, and G. Knörnschild, The Negative Difference Effect of Magnesium and of the AZ91 Alloy in Chloride and Stannate-Containing Solutions, *Corros. Sci.*, 2010, **52**, p 2235–2243

55. A. Madhan Kumar, S. Fida Hassan, A.A. Sorour, M. Paramsothy, and M. Gupta, Electrochemical Corrosion and In Vitro Biocompatibility Performance of AZ31Mg/Al$_2$O$_3$ Nanocomposite in Simulated Body Fluid, *J. Mater. Eng. Perform.*, 2018, **27**, p 3419–3428

56. M. Kumar, H. Dasarathy, and C. Riley, Electrodeposition of Brushite Coatings and Their Transformation to Hydroxyapatite in Aqueous Solutions, *J. Biomed. Mater. Res. A*, 1999, **45**, p 302–310

57. C. Chen, S. Qiu, S. Qin, G. Yan, H. Zhao, and L. Wang, Anticorrosion Performance of Epoxy Coating Containing Reactive Poly(*o*-phenylene-diamine) Nanoparticles, *Int. J. Electrochem. Sci.*, 2017, **12**, p 3417–3431

Publisher's Note Springer Nature remains neutral with regard to jurisdictional claims in published maps and institutional affiliations.